A census of dense cores in the Taurus L1495 cloud from the Herschel[*] Gould Belt Survey

K. A. Marsh[1]†, J. M. Kirk[2], Ph. André[3], M. J. Griffin[1], V. Könyves[3],
P. Palmeirim[3,4], A. Men'shchikov[3], D. Ward-Thompson[2], M. Benedettini[5],
D. W. Bresnahan[2], J. Di Francesco[6], D. Elia[5], F. Motte[3], N. Peretto[1],
S. Pezzuto[5], A. Roy[3], S. Sadavoy[7], N. Schneider[8,9], L. Spinoglio[5], G. J. White[10,11]

[1] *School of Physics and Astronomy, Cardiff University, Cardiff CF24 3AA, UK*
[2] *Jeremiah Horrocks Institute for Astrophysics and Supercomputing, University of Central Lancashire, Preston, PR1 2HE, UK*
[3] *Laboratoire AIM, CEA/DSM-CNRS-Université Paris Diderot, IRFU / Service d'Astrophysique, C.E. Saclay, Orme des Merisiers,*
91191 Gif-sur-Yvette, France
[4] *Laboratoire d'Astrophysique de Marseille, CNRS/INSU–Université de Provence, 13388 Marseille cedex 13, France*
[5] *Istituto di Astrofisica e Planetologia Spaziali - INAF, Via Fosso del Cavaliere 100, I-00133 Roma Italy*
[6] *National Research Council of Canada, Hertzberg Institute of Astrophysics, 5071 West Saanich Rd., Victoria, BC, V9E 2E7, Canada*
Paris-Sud 11, 91405 Orsay, France
[7] *Max-Planck-Institut für Astronomie (MPIA), Königstuhl 17, D-69117 Heidelberg, Germany*
[8] *Université Bordeaux, LAB, UMR 5804, 33270 Floirac, France*
[9] *CNRS, LAB, UMR 5804, 33270 Floirac, France*
[10] *Department of Physics and Astronomy, The Open University, Milton Keynes MK7 6AA, England*
[11] *Space Science and Technology Department, CCLRC Rutherford Appleton Laboratory, Oxfordshire OX11 0QX, England*

29 February 2016

ABSTRACT

We present a catalogue of dense cores in a $\sim 4° \times 2°$ field of the Taurus star-forming region, inclusive of the L1495 cloud, derived from *Herschel* SPIRE and PACS observations in the 70 μm, 160 μm, 250 μm, 350 μm, and 500 μm continuum bands. Estimates of mean dust temperature and total mass are derived using modified blackbody fits to the spectral energy distributions. We detect 525 starless cores of which $\sim$ 10–20% are gravitationally bound and therefore presumably prestellar. Our census of unbound objects is $\sim$ 85% complete for $M > 0.015 \, M_\odot$ in low density regions ($A_V \lesssim 5$ mag), while the bound (prestellar) subset is $\sim$ 85% complete for $M > 0.1 \, M_\odot$ overall. The prestellar core mass function (CMF) is consistent with lognormal form, resembling the stellar system initial mass function, as has been reported previously. All of the inferred prestellar cores lie on filamentary structures whose column densities exceed the expected threshold for filamentary collapse, in agreement with previous reports. Unlike the prestellar CMF, the unbound starless CMF is not lognormal, but instead is consistent with a power-law form below $0.3 \, M_\odot$ and shows no evidence for a low-mass turnover. It resembles previously reported mass distributions for CO clumps at low masses ($M \lesssim 0.3 \, M_\odot$). The volume density PDF, however, is accurately lognormal except at high densities. It is consistent with the effects of self-gravity on magnetized supersonic turbulence. The only significant deviation from lognormality is a high-density tail which can be attributed unambiguously to prestellar cores.

Key words: ISM: individual objects: L1495 — ISM: clouds — local interstellar matter — submillimetre: ISM — stars: formation — stars: luminosity function, mass function

1 INTRODUCTION

While much progress has been made in determining the form of the stellar initial mass function (IMF) (Chabrier 2003; Kroupa et al. 2013), a detailed explanation of its form and

possible environmental dependence must hinge on an understanding of the nature and evolution of the precursor cold dense cores. These cores are best observed in the sub-millimetre regime corresponding to their peak thermal dust emission; observations made with ground-based telescopes have previously helped to establish important links between the IMF and the prestellar core mass function (CMF) (e.g. Motte et al. 1998). With the advent of *Herschel*, however, these cores can now be studied with much higher sensitivity and hence the CMF can be probed to lower masses than before.

One of the major goals of the *Herschel* Gould Belt Survey (HGBS) (André et al. 2010) is to characterise the prestellar CMF over the Gould Belt. This survey covers 15 nearby molecular clouds which span a wide range of star formation environments. A principal product of the HGBS will be a catalogue, for each cloud, of all detected dense cores and protostellar objects. The first installment covers the Aquila molecular cloud; preliminary results were reported by Könyves et al. (2010) and the full Aquila catalogue is now available (Könyves et al. 2015). The present paper represents the next installment, which consists of a list of detected dense cores in a portion of the Taurus Molecular Cloud containing L1495. This catalogue is available for download in the electronic edition of this paper. A portion is shown in Appendix B to illustrate the format and content.

The Taurus cloud represents a nearby region of predominantly non-clustered low-mass star formation, at an estimated distance of 140 pc (Elias 1978), in which the stellar density is relatively low and objects can be studied in relative isolation. Its detailed morphology at *Herschel* wavelengths is discussed by Kirk et al. (2013). Overall, it is dominated by two long ($\sim 3°$), roughly parallel filamentary structures, the northern of which is the larger. Early results from *Herschel* regarding the filamentary properties have been reported by Palmeirim et al. (2013). The catalogue presented here covers the L1495 cloud located in the western portion of the northern filamentary structure, designated as N3 in Kirk et al. (2013).

2   OBSERVATIONS

The observational data on which the present catalogue is based consists of a set of images of the L1495 cloud in the Taurus star-forming region, made as part of the HGBS[1] (André et al. 2010). The data were taken using PACS (Poglitsch et al. 2010) at 70 μm and 160 μm and SPIRE (Griffin et al. 2010) at 250 μm, 350 μm, and 500 μm in fast-scanning (60 $''\mathrm{s}^{-1}$) parallel mode. The North-South scan direction for L1495 was split into two observations taken on 12 February 2010 and 7 August 2010, while the East-West cross-scan direction was observed in a single run on 8 August 2010. The corresponding *Herschel* Observation IDs are 1342202254, 1342190616, and 1342202090. An additional PACS observation (Observation ID 1342242047) was taken on 20 March 2012 in the orthogonal scan direction to fill a gap found in the previous PACS data.

Calibrated scan-map images at the PACS wavelengths

were produced in the HIPE Version 10 pipeline (Ott 2010) using Scanamorphos Version 20 (Roussel 2013). The SPIRE images were produced in the same pipeline using the "naive" map-making procedure and the destriper module. The arbitrary sky offset values were corrected by comparison with Planck and *IRAS* data using a procedure similar to that employed by Bernard et al. (2010). The estimated offset values[2] for SPIRE correspond well to the ones determined from the zero-point correction task in HIPE. The spatial resolution values (FWHM beamsizes) of these maps are approximately 8.5$''$, 13.5$''$, 18.2$''$, 24.9$''$, and 36.3$''$ in the 70 μm, 160 μm, 250 μm, 350 μm, and 500 μm wavelength bands, respectively. In the PACS bands, however, the effective beams resulting from fast scanning are somewhat elongated, at $\sim 6'' \times 12''$ (70 μm) and $\sim 12'' \times 16''$ (160 μm). The present catalogue is based on a rectangular subregion of size $\sim 4° \times 2°$, whose long axis is aligned approximately with the axis of the long filamentary structure at a position angle of $-52°$.

3   SOURCE DETECTION AND CLASSIFICATION

The production of the catalogue of cores for all of the various star-forming regions within the Gould Belt represents a parallel effort by a number of groups. To ensure uniformity, all groups are adhering strictly to the procedure specified in detail by Könyves et al. (2015). The identification of starless cores is then essentially a two-step process:

Step 1: Detection: Source detection is carried out using the *getsources* algorithm (Men'shchikov et al. 2012) as provided by the Nov. 2013 major release (Version v1.140127). Starless core candidates are detected while making simultaneous use of images in the four *Herschel* wavebands in the 160–500 μm range, the 160 μm image being a temperature-corrected version (see Könyves et al. 2015 for details). In addition, a column density map is used as if it were an additional waveband, the purpose being to give extra weight to regions of high column density. This map[3], with an effective spatial resolution of 18.2$''$ corresponding to the 250 μm beam, is obtained using the technique described in Appendix A of Palmeirim et al. (2013). The output of the detection step consists only of sources deemed "reliable" on the basis of the *getsources* "global goodness" parameter, which combines the global detection significance, the combined signal-to-noise ratio (S/N) over all bands, and source geometry knowledge.

As discussed by Könyves et al. (2015), the detection of cores is carried out separately from that of protostellar objects, the latter being based on a second run of *getsources* in which detection is based on the 70 μm data only. The *Herschel* results for protostellar objects in this region will be discussed separately (J. M. Kirk et al., in preparation).

Step 2: Classification:

Classification as a starless core candidate requires that all of the following conditions be met:

(i) column density detection significance greater than 5 (where significance in this case refers to detection at the relevant single spatial scale, as defined by Men'shchikov et al. 2012);

(ii) column density $(S/N)_{peak} > 1$ at $18.2''$ resolution;

(iii) global detection significance over all wavelengths (Men'shchikov et al. 2012) greater than 10;

(iv) flux detection with significance greater than 5 for at least two wavelengths between 160 μm and 500 μm;

(v) flux measurement with $S/N > 1$ in at least one band between 160 μm and 500 μm for which the monochromatic detection significance is greater than 5;

(vi) detection significance less than 5 for the 70 μm band *or* 70 μm peak flux per pixel less than zero *or* source size (full width at half maximum, FWHM) at 70 μm larger than 1.5 times the 70 μm beam size;

(vii) source not spatially coincident with a known galaxy, based on comparison with the NASA Extragalactic Database (NED) or with a known young stellar object (YSO) based on the published list of Widefield Infrared Survey Explorer (WISE) detections (Rebull et al. 2011);

(viii) source appears real based on visual examination of the SPIRE images and column density maps.

Imposition of the last criterion is facilitated by examination of the "summary card" for each source, included as one of the on-line catalogue products[4]. It includes a cutout column density image of the source, upon which is superposed the elliptical 50% contour as estimated by *getsources*. To provide some additional confidence in the reality of the extracted source, the subimage is also superposed with a source ellipse estimated by an entirely different source extraction technique, namely the Cardiff Source-finding AlgoRithm (CSAR) discussed in Appendix B of Kirk et al. (2013). The latter was run on the high-resolution ($18.2''$) column density map. The above procedure resulted in 525 objects classified as starless cores, of which 46% were detected by CSAR[5]. Their locations are shown in Fig. 1 relative to a column density image of the field produced by the Palmeirim et al. (2013) technique.

Although most of the sources in Fig. 1 are clearly associated with filamentary structure in L1495, we cannot rule out the possibility that a few of them may be extragalactic contaminants. Some extragalactic sources may, in fact, have been missed in the NED as a result of foreground confusion by Taurus itself. To assess this possibility we note that the estimated rms level of extragalactic contaminants

---

[4] These ancillary data consist of the full catalogue, a table of derived parameters, and the set of summary cards. They are available in the on-line version of this paper, and from the HGBS website at http://gouldbelt-herschel.cea.fr/archives. Also available from the latter link are all of the HGBS data products, which include *Herschel* images and the column density and dust temperature maps.

[5] A source detected by *getsources* is considered to have a CSAR counterpart if the CSAR position falls within the 50% elliptical contour of the high-resolution column density map as measured by *getsources*.
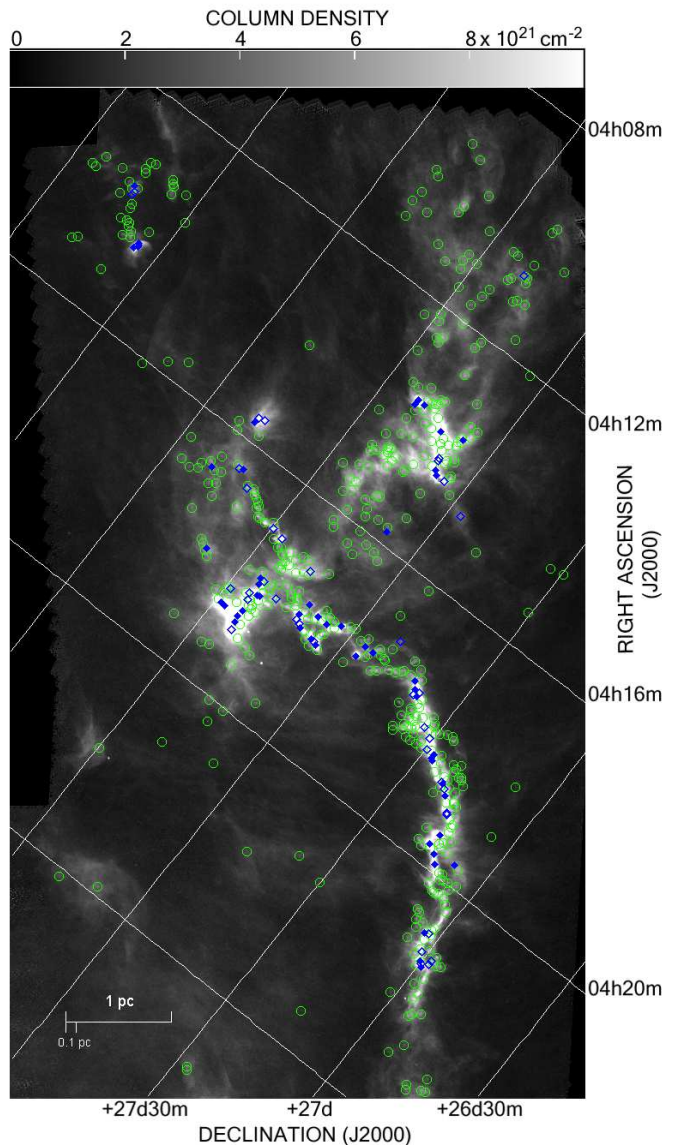

Figure 1. Column density map of the region studied. The spatial resolution is approximately $18.2''$ and the column density units are hydrogen molecules per cm^2. The overplotted symbols represent the locations of detected cores (green circles = unbound starless, filled blue diamonds = prestellar, open blue diamonds = candidate prestellar). The peak column density is 5.5×10^{22} cm^{-2}, although the display scale is truncated at 1.0×10^{22} cm^{-2} to improve the visibility of faint features.

is < 10 mJy in *Herschel* bands between 160 μm and 500 μm (Garcia-Lario et al. 2014), more than an order of magnitude lower than that of 99% our detected cores. Nevertheless, some extragalactic sources may be present in the remainder.

4 ESTIMATES OF CORE MASSES AND TEMPERATURES

Estimates of the core masses and dust temperatures were obtained for each source by fitting a modified blackbody spectrum to the observed spectral energy distribution (SED)

constructed from the set of *getsources* flux densities in the wavelength range 160–500 μm. The SED point at each wavelength represents the flux density integrated over the entire source, and overlapping sources are deblended as described by Men'shchikov et al. (2012). The flux densities used in SED fitting are presented in Table B1. For this exercise, sources were assumed to be isothermal and have a wavelength variation of opacity of the form (Hildebrand 1983; Roy et al. 2014):

$$\kappa(\lambda) = 0.1 \, (300/\lambda)^2 \qquad \text{cm}^2\,\text{g}^{-1} \qquad (1)$$

where λ is the wavelength in μm. The fitting procedure used was the same as that described by Könyves et al. (2015), and involved a weighted least squares fit in which each SED flux was weighted by the inverse square of its measurement uncertainty, as estimated by *getsources*. Those uncertainties are dominated by errors associated with background subtraction.

The fits were based on an assumed distance of 140 pc. Following Könyves et al. (2015), the 500 μm flux was excluded from the fit in the small minority of cases in which this flux exceeded that at 350 μm, as a precaution against confusion contamination at the longer wavelength.

Some of the detected cores can be expected to be gravitationally bound, and thus likely to go on to form stars. We therefore refer to the members of this subset as prestellar cores, and identify them by modelling the sources as Bonnor-Ebert (B-E) spheres (Bonnor 1956; Ebert 1955). For a source of outer radius R, the B-E critical mass (Bonnor 1956) is given by:

$$M_{\mathrm{BE}} = 2.4 \, R \, a_s^2 / G \qquad (2)$$

where G is the gravitational constant and a_s is the isothermal sound speed. The latter is given by $a_s = (kT/\mu)$ where k is Boltzmann's constant and T is the gas temperature which we equate with the estimated dust temperature.

The correspondence between R and the source size estimated using *getsources* has been investigated by Könyves et al. (2015). Briefly, simulations of *getsources* extractions on a set of B-E source models show that the *getsources* FWHM values provide good measurements of the outer radii of critical B-E spheres (with an accuracy better than 10-20%) if spatially well resolved. For marginally-resolved cores, the *getsources* FWHM estimate provides a reliable estimate of the true B-E radius after convolution with the beam. For cores with extended power-law wings, however, the source sizes are not measured as reliably by the current version of *getsources*. Based on these considerations we take R as the geometric mean of the source FWHM major and minor axes as estimated by *getsources* from the column density map made at 18.2″ resolution, after simple beam deconvolution (quadrature subtraction of the beam FWHM).

Following André et al. (2007) and Könyves et al. (2015), we then classify a detected starless core as "prestellar" if its estimated mass exceeds $M_{\mathrm{BE}}/2$ (cf. Bertoldi & McKee 1992). The factor of 2 corresponds to the value of the virial ratio below which an object would be regarded as gravitationally bound, taking M_{BE} as a proxy for the virial mass. Since the mass threshold depends linearly on R, misclassification is likely for many marginally-resolved sources. In order to avoid rejecting genuine prestellar cores

in that category entirely, we provide an additional list of "candidate prestellar cores" which, although lacking sufficient mass for robust classification as prestellar, nevertheless remain plausible candidates. We select them by lowering the threshold value of M/M_{BE} from 0.5 (well-resolved cores) down to 0.2 (marginally-resolved cores). The actual functional dependence of the threshold, t, on angular source size has been estimated, in the case of the Aquila region, by Könyves et al. (2015) using simulations. They obtained $t = 0.2 \, (\theta_{\mathrm{source}}/\theta_{\mathrm{beam}})^{0.4}$ subject to $0.2 \leqslant t \leqslant 0.5$, where θ_{source} and θ_{beam} represent the FWHMs of source and beam in the high-resolution column density map. Our Taurus simulations, conducted in connection with the completeness estimates described in Appendix A, suggest that the latter expression is appropriate here also.

Fig. 2 shows a plot of estimated mass, M, versus radius, R. The plotted points are distinguished based on their gravitational status, i.e., bound, possibly bound (candidate prestellar), or unbound. Also plotted for comparison are previous Taurus data from the literature. Clearly, the masses and radii are well correlated and are consistent with the power-law relation found from previous studies of dense cores and clumps in molecular clouds (e.g., Larson 1981; Kauffmann et al. 2010). They are also consistent with extinction-based results for L1495 (Schmalzl et al. 2010), $C^{18}O$ (Onishi et al. 1996), $H^{13}CO^+$ (Onishi et al. 2002), and with the Kirk et al. (2013) results for other parts of the Taurus molecular cloud (the Barnard 18 and L1536 clouds) based on *Herschel* data, and with NH_3 data (Benson & Myers 1989).

Fig. 3 shows a plot of dust temperature versus mean column density and indicates that these quantities are negatively correlated. Such a correlation might be expected based on a model in which the dust is heated by the interstellar radiation field (ISRF). Large column densities then provide more shielding, resulting in cooler dust (Evans et al. 2001; Stamatellos et al. 2007; Roy et al. 2014). But could this correlation be an artifact, induced by a degeneracy between mass and temperature in the SED measurement model? Such a degeneracy is certainly possible in cases of limited wavelength coverage, particularly if the observed wavelengths are all on the Rayleigh-Jeans side of the Planck peak for the particular dust temperature. For the present observations, however, the *Herschel* wavelengths bracket the peak of the modified blackbody function for all of the core temperatures likely to be encountered. It is true that temperature gradients within cores can also give rise to mass biases (and hence column density biases) when using simple SED fitting, but these biases are typically at the $\lesssim 30\%$ level (see, for example, Roy et al. 2014; Könyves et al. 2015) and not sufficient to produce the correlation apparent in Fig. 3. Furthermore, the latter correlation remains even after full account is taken of the effects of radial temperature gradients (Marsh et al. 2014). We thus conclude that the correlation is real, and consistent with the ISRF heating model (Stamatellos et al. 2007).

The temperature versus mass plot of Fig. 4 shows that these quantities are at least partially correlated in the sense that the more massive cores ($M \gtrsim 1\,M_\odot$) have the lowest temperatures. There is, however, no information as to whether the converse is true; the detection sensitivity cutoff prevents us from knowing whether all low mass cores
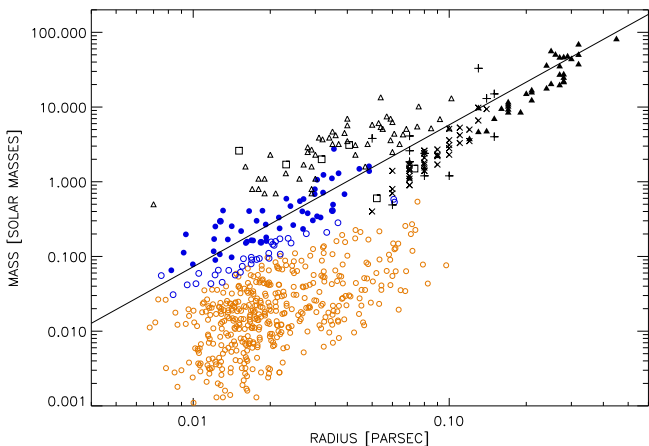
Figure 2. The mass-radius correlation for cores in Taurus. The coloured symbols represent our estimates of core mass as a function of deconvolved radius for the L1495 sources classified as starless cores. Blue filled circles, blue open circles, and gold open circles represent prestellar cores, candidate prestellar cores, and gravitationally unbound starless cores, respectively. Black symbols represent previously published Taurus data, as follows: *Squares*: Observations at 850 μm (Kirk et al. 2005); "×": Extinction-based measurements of cores in L1495 (Schmalzl et al. 2010); *Filled triangles*: Estimates based on $C^{18}O$ observations (Onishi et al. 1996); *Open triangles*: Estimates based on $H^{13}CO^+$ observations (Onishi et al. 2002); "+": Estimates based on NH_3 observations (Benson & Myers 1989). Also shown for comparison (solid line) is the mass-radius relation for clumps in molecular clouds (Larson 1981), represented by $M/M_\odot = 460\,R_{[pc]}^{1.9}$.
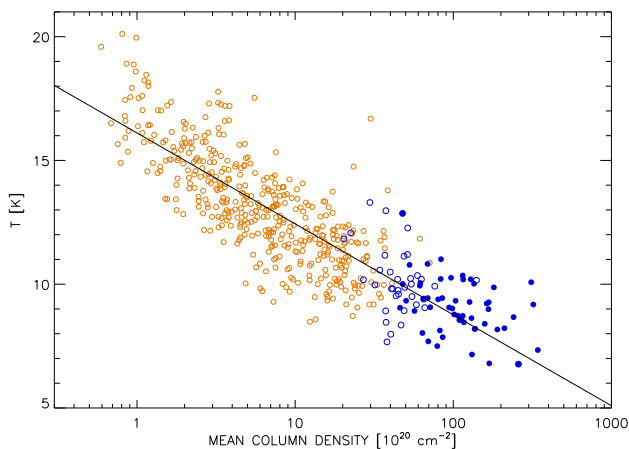

Figure 3. Estimated mean dust temperature plotted as a function of mean core column density, $N_{H_2} = M/(\pi R^2 \mu m_H)$, where μ is the mean molecular weight (taken as 2.8) and m_H is the mass of a hydrogen atom. Blue filled circles, blue open circles, and gold open circles represent prestellar, candidate prestellar, and unbound starless cores, respectively. The straight line represents a linear regression fit to all of the points, and corresponds to a $T[K]$ versus $N_{H_2}[10^{20}\,cm^{-2}]$ relation of the form $T = -3.6\log_{10} N_{H_2} + 16.1$. This correlation can be expected to be region-dependent due to its likely dependence on the local ISRF.
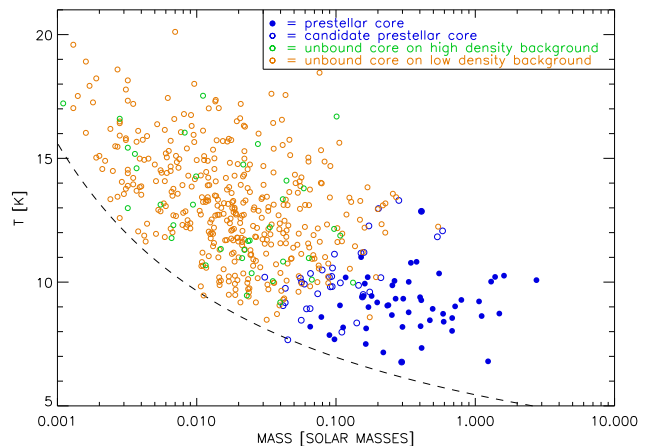

Figure 4. Estimated mean dust temperature plotted as a function of estimated core mass. Bound (prestellar) cores and prestellar core candidates are plotted as filled and open blue circles, respectively. Unbound cores are represented by open circles and are divided into those seen against high column density backgrounds characterised by $A_V > 7$ mag (green symbols), and more diffuse backgrounds (gold symbols). The dashed line represents the detection limit, i.e., the lowest detectable mass for a given core temperature.

have high temperatures. Therefore, although this figure indicates that, within the detected population, unbound starless cores have systematically higher temperatures than prestellar cores, we cannot rule out the existence of a population of cool starless cores. This issue is discussed further in Appendix A.

5 OVERALL STARLESS CORE MASS FUNCTION

The dashed red histogram in Fig. 5 represents the uncorrected mass distribution for the sample as a whole, without regard for inferred gravitational status (bound or unbound). One feature of this distribution is an apparent decrease in source counts for masses below $\sim 0.01\,M_\odot$, in the mass regime dominated by unbound starless cores. However, comparison with the completeness curve for unbound cores (Appendix A) suggests that this behaviour may be an effect of incompleteness. Although the detailed form of the completeness curve is subject to uncertainty as discussed in Appendix A, it is nevertheless instructive to apply it as a correction to the raw CMF to get an indication of how the true starless CMF may look. The result is shown by the solid red histogram in Fig. 5. We conclude that there is no evidence for a low-mass turnover in the starless CMF in the range surveyed by *Herschel* and that the overall starless CMF probably continues to rise towards even lower masses. This result means that the apparent turnovers in previous estimates of the Taurus CMF (for example, the submillimetre-based estimate of Sadavoy et al. 2010 and the extinction-based estimate of Schmalzl et al. 2010) were due to the incompleteness of those surveys. In the case of the Sadavoy et al. (2010) survey, some of the incompleteness in the overall starless core population can be attributed to the fact that ground-
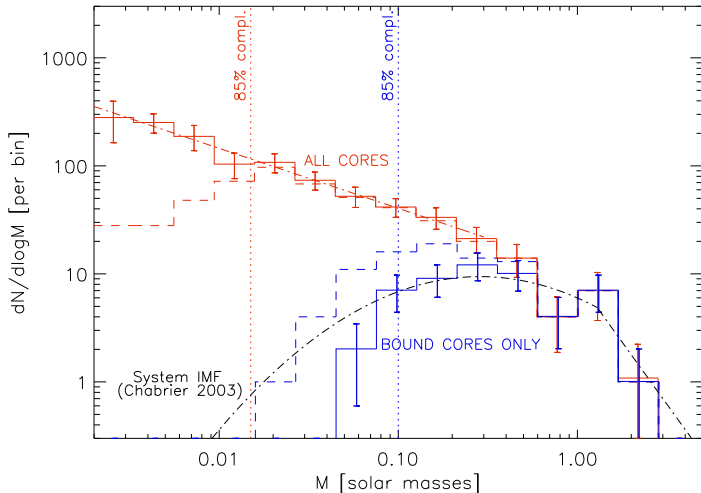
Figure 5. Estimated core mass function. The dashed red histogram shows the CMF for the complete set of detected cores, uncorrected for the incompleteness of the observations. Applying an approximate correction for incompleteness, based on the results in Appendix A, yields the solid red histogram. The dash-dot red line represents a function of the form $dN/d\log M \propto M^{-0.55}$, obtained by linear regression of the logarithmic variables in the mass range $M/M_\odot < 0.3$. The solid blue histogram shows the gravitationally bound (i.e., prestellar) subset, while the dashed blue histogram represents the subset consisting of some additional *candidate* prestellar objects. In neither case has any correction been applied for incompleteness. The vertical dotted lines represent the 85% completeness limits for unbound starless cores (red) and prestellar cores (blue), as discussed in Appendix A. Also shown for comparison (black dash-dot curve) is a scaled version of the Chabrier (2003) system IMF in which masses have been scaled upwards by a factor of 1.3.

based 850 μm observations preferentially select the *densest* objects, i.e., those most likely to be prestellar, for reasons discussed by Ward-Thompson et al. (in preparation). In any event, the *Herschel* observations have served to extend the overall starless CMF, as derived from dust emission, by an order of magnitude in mass below that of previous estimates.

In the mass range dominated by unbound cores ($M \lesssim 0.3\,M_\odot$), the CMF in Fig. 5 is consistent with power-law behaviour, i.e., $dN/d\log M \propto M^\alpha$. A linear regression with respect to the logarithmic quantities then yields the maximum likelihood estimate $\alpha = -0.55 \pm 0.07$. This is consistent with the observed power-law distribution of CO clumps, for which a representative value of α is -0.7 ± 0.1 based on the collective data for a number of star-forming regions (Kramer et al. 1998). Such clumps are the relatively low density structures previously detected in CO emission, the majority of which are gravitationally unbound (Blitz 1993; Kramer et al. 1998). As with the *Herschel* unbound cores, the CO clump distribution shows no low-mass turnover (Kramer et al. 1998). Clumps identified by various isotopologues of CO all show fairly similar slopes in their mass distributions at low masses. For example, observations of the Perseus molecular cloud give α values of -0.36 ± 0.08 ($0.1 < M/M_\odot < 3$) and -0.4 ± 0.2 ($0.03 < M/M_\odot < 5$) for $C^{18}O(3\text{-}2)$ and $^{13}CO(3\text{-}2)$ (Curtis 2009), respectively, both

of which are consistent with our estimate based on dust emission for the mass ranges in common. The maps of $C^{18}O$ are, in fact, strikingly similar to those in the 850 μm continuum (Curtis et al. 2010), suggesting that similar densities of material are being traced. It seems likely, therefore, that our unbound starless cores represent the dust-emission counterparts of the $C^{18}O$ clumps.

The Curtis (2009) observations also revealed a population of $C^{18}O$ clumps with no 850 μm counterparts. These were low-mass objects which subsequent virial analysis showed to be gravitationally unbound. Similar behaviour was found in ρ Oph by White et al. (2015). Their lack of detection at 850 μm was due, at least in part, to the fact that the 850 μm observations were not sensitive to masses below about 0.1 $M_\odot$. The *Herschel* data will allow such analyses to be extended to lower masses and provide further elucidation of the nature of gravitationally unbound cores.

6   THE PRESTELLAR CORE SUBSET

We find that 52 of our 525 starless cores fulfil the requirements for robust classification as gravitationally bound, i.e., prestellar, based on the criteria listed in Section 4. An additional 38 cores may be regarded as candidate (non-robust) detections of prestellar cores based on the somewhat more relaxed criteria specified in that section. The total number of prestellar cores in the starless sample is therefore somewhere in the range 52–90, representing ~ 10–20% of the starless core sample. This represents a significant difference with respect to the Aquila region, for which the bound fraction of *Herschel* cores is $\sim 60\%$ (Könyves et al. 2015). The CMFs of the robust and candidate subsets of bound cores are shown by the solid and dashed blue histograms, respectively, in Fig. 5. There may well be even more prestellar cores whose masses fall below the completeness limit of $\sim 0.1\,M_\odot$. Such a possibility is raised by the previous interferometric detection of a pre-brown dwarf candidate in Ophiuchus/L1688 (André et al. 2012) whose mass, $\sim 0.02\,M_\odot$, falls well below the *Herschel* completeness limit.

Above the completeness limit, the prestellar CMF is consistent with lognormal form and resembles the Chabrier (2003) estimate of the stellar system IMF, consistent with previous findings for other star-forming regions (Alves et al. 2007; Simpson et al. 2008; André et al. 2010). Those studies did, however, find that to reconcile the CMF with the IMF, scaling was required on the mass axis, and the scaling factor was interpreted in terms of the star formation efficiency based on a simple model in which each core gives rise to one stellar system. We estimate the scaling factor by multiplying the mass axis of the Chabrier (2003) IMF by various factors, and selecting the value which minimises the weighted sum of squares of residuals with respect to the observed CMF. The weighting used is inverse-variance, based on the Poisson error bars of the observed CMF values. The optimal scaling factor is then 1.3, but given the large statistical uncertainties due to the relatively small number of prestellar cores, the data are consistent with values ranging from ~ 1 to ~ 2. Hence there is no evidence for star formation efficiencies which differ significantly from the value $\sim 40\%$ reported for Aquila (Könyves et al. 2015). These conclusions are un-

changed if the Chabrier (2003) system IMF is replaced by those of Kroupa et al. (2013).

Errors in our estimated CMF can arise from a number of effects. As mentioned earlier, the non-isothermal structure of cores has an effect on masses estimated by the simple SED fitting procedure used here. As discussed by Könyves et al. (2015), the masses can be underestimated by factors ranging from $\sim 20\%$ to ~ 2 depending on the column density (and hence, indirectly, the mass) of the core. Consequently, the number of cores classified as prestellar is reduced. The masses may be further underestimated due to the underestimation of outer radii for cores with developed power-law wings. More detailed modelling of the temperature and density structure would alleviate these effects, but in the meantime we cannot say conclusively that the prestellar CMF in L1495 is of lognormal form, but only that it is consistent with that form given the current level of uncertainty.

6.1 Relationship to filaments

Herschel observations have provided strong indications of an evolutionary link between filaments and cores (André et al. 2010, 2014), and so it is of interest to ask what fraction of prestellar cores lies on filaments. In this regard Polychroni et al. (2013) found that 71% of prestellar cores in the L1641 cloud of Orion A were located on filaments with $A_V > 5$ mag, leaving a substantial fraction that were not. This may be compared with the early estimate of $> 60\%$ for the fraction on supercritical filaments in Aquila (André et al. 2010) and the more recent (and more robust) estimate of $75^{+15}_{-5}\%$ by Könyves et al. (2015).

There is no common consensus in the literature regarding the definition of a filament. Most definitions are observationally based and therefore quite subjective. To provide a context for subsequent discussion, we adopt as a working definition the one given by André et al. (2014), i.e., "any elongated ISM structure with an aspect ratio larger than ~ 5–10 that is significantly overdense with respect to its surroundings," but qualify it further by specifying that the elongated structure must be visible directly in a column density image that has not been spatially filtered.

To investigate the situation for L1495, we compare the locations of our inferred prestellar cores with the background filamentary structure extracted using the recently developed *getfilaments* algorithm (Men'shchikov 2013). The latter is similar to *getsources* in that it involves filtering at a range of spatial scales. Fig. 6 shows the results obtained from the L1495 column density map. It represents a reconstruction of elongated structures up to a transverse spatial scale of 145″ which, at 140 pc, corresponds to the 0.1 pc characteristic filamentary width found in previous studies (Arzoumanian et al. 2011; Palmeirim et al. 2013). Note that the spatial filtering has suppressed the broad power-law wings revealed by those studies. The wings actually extend considerably further out than the 0.1 pc corresponding to the FWHM of the cross-sectional profile. The spatial filtering does, however, serve to show the smaller scale features superposed on the overall filament structure. Some of these features are in the form of threadlike structures which correspond very well to the velocity coherent "fibres" identified by Hacar et al. (2013) in $C^{18}O$ (see Fig. 2 of André et al. 2014). We will use the term "filamentary structure" to include both the large-scale filaments and the smaller-scale fibres.

Superposed on Fig. 6 are the core locations. We find that 100% of the prestellar cores are located on filamentary structure with $A_V \geqslant 5$ mag, as opposed to 40% for the starless core sample as a whole. A similarly strong correlation was found between YSO locations and filamentary structure in Taurus by Doi et al. (2015). Fig. 7 shows a histogram of total background column density values at the locations of the prestellar cores. It is prominently peaked at $\sim 1.3 \times 10^{22}$ cm^{-2} and indicates that 90% of the column densities exceed 5.9×10^{21} cm^{-2}. The latter, which may be interpreted as an approximate lower threshold for star formation, is consistent with the value $\sim 7 \times 10^{21}$ cm^{-2} for Aquila (André et al. 2014; Könyves et al. 2015) and also with the threshold found by Goldsmith et al. (2008) for Taurus young stars. If we take 0.1 pc as the mean filamentary width, then the estimated line masses of filamentary structure in the immediate vicinities of prestellar cores throughout L1495 are in the range 32 ± 15 $M_\odot$ pc^{-1}. Our mean value is about a factor of two larger than the value 15 $M_\odot$ pc^{-1} found by Hacar et al. (2013) using N_2H^+ observations, and the value 17 $M_\odot$ pc^{-1} found by Schmalzl et al. (2010) based on near-infrared extinction measurements. The reason for the discrepancy is not clear, but it is significant that all three estimates are greater than or equal to the theoretical value of 16 $M_\odot$ pc^{-1} for an isothermal cylinder in pressure equilibrium at 10 K (Inutsuka & Miyama 1997). This suggests that all of the prestellar cores in L1495 are located in supercritical filaments, in agreement with the HGBS findings in Aquila (André et al. 2010; Könyves et al. 2015). We note that none of the above estimates includes the contribution of the extended power-law wings whose inclusion further increases the estimated line mass. For example, the line mass integrated over the full filamentary cross section of the B211 filament is estimated to be 54 $M_\odot$ pc^{-1} (Palmeirim et al. 2013).

6.2 Relationship to unbound starless cores

While the majority of our starless cores are gravitationally unbound and therefore not prestellar, they nevertheless can provide some important information relevant to star formation. For example, they may represent density enhancements resulting from the interstellar turbulence widely considered to play a dominant role in the determination of the IMF (see, for example, Padoan & Nordlund 2002; Hennebelle & Chabrier 2008). The probability distribution function (PDF) of the gas density produced by supersonic turbulent flow of isothermal gas is well approximated by a lognormal form (Elmegreen & Scalo (2004) and references therein). It is therefore of interest to plot a histogram of estimated density values for the L1495 starless cores, and this histogram is shown in Fig. 8. These densities are mean values, calculated by dividing the mass of each core by its total volume, based on the estimated outer radius, taken to be the deconvolved FWHM of the source. These densities also correspond to the $n(H_2)$ values listed in Table B2 of Appendix B. It is evident that, in sharp contrast to the CMF, the volume density distribution is accurately lognormal except for a tail at high densities. A maximum likelihood fit for $3 \times 10^2 \leqslant n(H_2)[cm^{-2}] \leqslant 3 \times 10^4$ gives a reduced chi
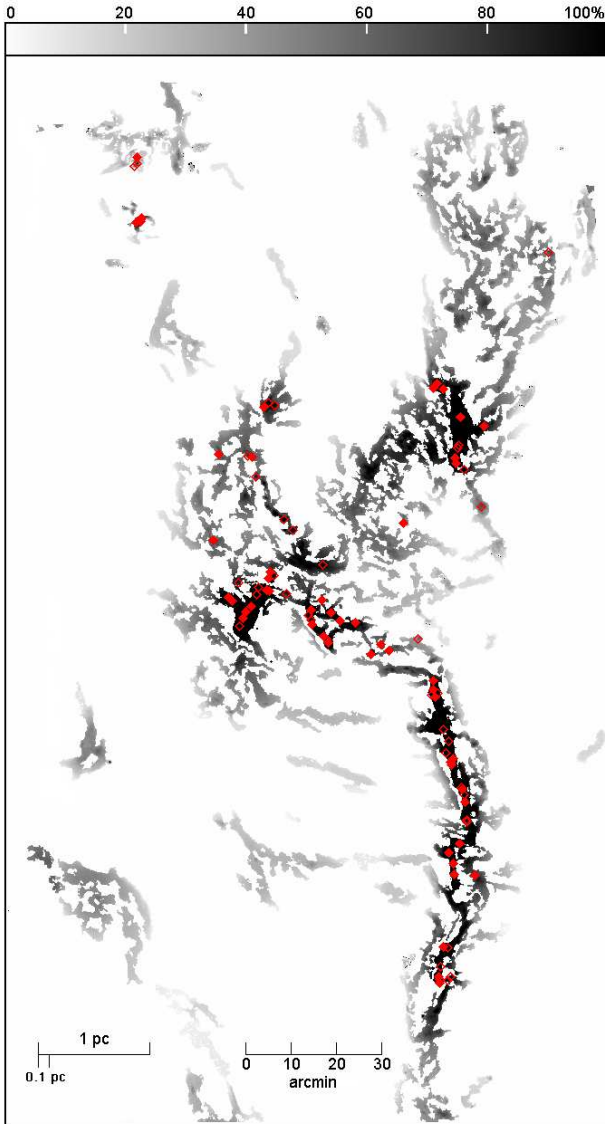
Figure 6. The locations of prestellar cores (filled red diamonds) and additional prestellar core candidates (open red diamonds) with respect to filamentary structure, shown with the same field of view as for Fig. 1. The image has been rotated such that equatorial north is 52° anticlockwise from vertical. The filamentary structure represents a limited-scale reconstruction, up to a transverse spatial scale of 0.1 pc, obtained using the *getfilaments* algorithm (Men'shchikov 2013). The greyscale values correspond to the *total* (unfiltered) background line densities within the boundaries of the reconstructed features, based on an assumed characteristic filamentary width of 0.1 pc, and are truncated at an upper value corresponding to 16 $M_\odot \, \mathrm{pc}^{-1}$ (100% on the greyscale). As a result, the portions in black have a mass per unit length in excess of the approximate threshold for cylindrical stability.

squared value of 0.95, indicating complete consistency with a lognormal function.

In deriving Fig. 8 it was necessary to make allowance for incompleteness since low-mass cores ($M < 0.01\,M_\odot$) make a significant contribution to the peak of the histogram. We therefore applied the same incompleteness correction as for the starless CMF in Fig. 5. In order to investigate the sen-
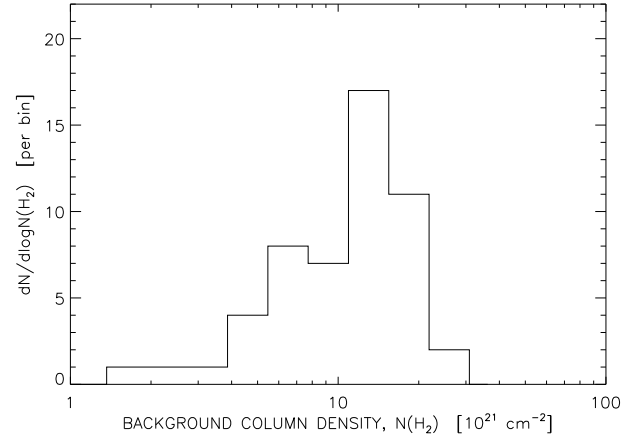

Figure 7. The distribution of filamentary background column densities associated with prestellar cores.
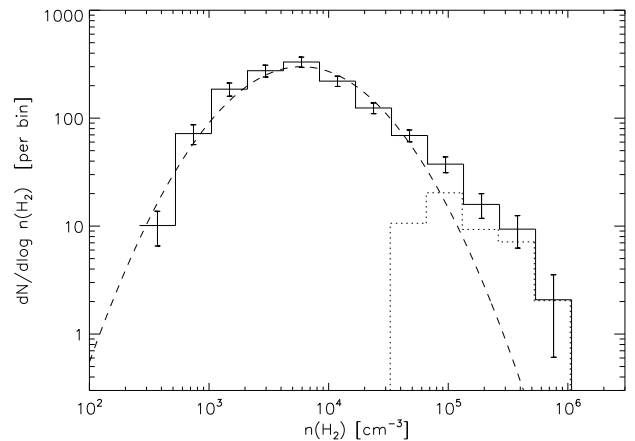

Figure 8. Histogram of estimated gas density of the starless cores (solid line). The dotted line represents the "prestellar" subset, i.e., the gravitationally bound cores. For comparison, the dashed line represents a lognormal with a standard deviation of 1.2 in $\ln n(\mathrm{H_2})$. The error bars are based on Poisson statistics with respect to the number in each bin.

sitivity to this correction, we have also derived an alternate version based on a low-mass extrapolation of the "complete" portion of the observed CMF in Fig. 5, the key assumption being that the true CMF of unbound starless cores is of power-law form. An almost identical result was obtained, indicating that the shape of the estimated volume density histogram is not strongly dependent on the specific assumptions made regarding incompleteness.

The variance in log density may provide information on the kinetic energy injection mechanism, the Mach number, and the magnetic field (Molina et al. 2012). To compare Fig. 8 with turbulence models, however, it must be borne in mind that what we have plotted is essentially a type of mass-weighted PDF, as opposed to the volume-weighted version usually presented in simulations. More quantitatively, if we make the simplifying assumption that the density is uniform within an individual core (as would be the case for

pressure-confined clumps[6] that probably form the bulk of the unbound core distribution) and assume a mass-radius law of the form $M \propto R^k$, then the core density histogram of Fig. 8 can be represented as a PDF, $P_C(\rho)$, which is related to the volume-weighted version, $P_V(\rho)$, by:

$$P_C(\rho) \propto \rho^{3/(3-k)} P_V(\rho) \qquad (3)$$

where ρ is the density. Furthermore, the assumption of log-normal form for $P_V(\rho)$ means that $P_C(\rho)$ is also a lognormal with the same variance in log density, but with a higher mean density, ρ_0. It is possible that our density histogram is somewhat narrower than the true mass-weighted PDF since it does not include the low density background component. This is probably not a large effect, however, since in transforming the volume-weighted PDFs (as presented, for example, by Molina et al. 2012) to their mass-weighted counterparts, the low-density background component is de-emphasised. Despite this, the variance of the distribution is unchanged by the transformation, as illustrated by Fig. 6 of Ginsburg et al. (2013). This enables Fig. 8 to be compared with previously published simulations and theory.

Using the customary notation $s \equiv \ln(\rho/\rho_0)$, our observations then yield a standard deviation, σ_s, of 1.2 ± 0.1, which is consistent with simulations of magnetized (MHD) turbulence obtained by Molina et al. (2012) for Mach numbers, $\mathcal{M}$, in the range ~ 5–10. In those simulations, however, unmagnetized supersonic turbulence results in an asymmetric low-density tail to the distribution which is not evident in Fig. 8. The absence of such a tail seems to argue for the moderating influence of a magnetic field.

The above value of σ_s may also be compared with the results of a recent study of the turbulence-driven density distribution in a non-star-forming cloud comprised of G43.17+01 and G43.16−0.03 by Ginsburg et al. (2013), who obtained $1.5 < \sigma_s < 1.9$ and used the result to constrain the compressive part of the driving force. The importance of the latter study is that it focused on turbulence at the pre-star-forming stage of the cloud, essentially unaffected by gravity. A more detailed comparison of the PDFs of L1495 and G43.17+01/G43.16−0.03 may therefore provide evolutionary information on the density structures.

The one major deviation from lognormality in Fig. 8 is the presence of the high-density tail in the distribution. We attribute this tail to the gravitational collapse of cores at the high density end. This interpretation is confirmed by restricting the plot to prestellar cores only, as indicated by the dotted line in the figure. Such behaviour is predicted by simulations (Kritsuk et al. 2011; Collins et al. 2012; Federrath & Klessen 2013) which yield model PDFs similar in appearance to Fig. 8.

The core density above which gravity becomes dominant, i.e., the point, n_{dev}, at which the histogram in Fig. 8 deviates from lognormal behaviour, is $\sim 10^5\,\text{cm}^{-3}$. A similar situation can be inferred in Aquila (Könyves et al. 2015), whereby the volume density PDF shows the tentative presence of a power-law tail above $\sim 10^5\,\text{cm}^{-3}$. The importance of the deviation value is that it can be related directly to

the background volume density threshold for star formation, n_{crit}, a quantity which so far has been difficult to obtain observationally (Kainulainen et al. 2014). The relationship is based on the fact that the volume density contrast of a critical B-E sphere over the background is ~ 2.4 (cf. André et al. 2007). We thereby estimate $n_{\text{crit}} \sim 4 \times 10^4\,\text{cm}^{-3}$.

The above value may be compared with the expected threshold based on the collapse of supercritical filaments, as discussed by André et al. (2014). Specifically, the critical line mass of 16 $M_\odot\text{pc}^{-1}$, together with the characteristic filamentary width of 0.1 pc, implies a critical number density $n_{\text{H}_2} \sim 2 \times 10^4\,\text{cm}^{-3}$. This is consistent with our n_{crit} estimate, given the factor of ~ 2 uncertainty in the latter. Our estimate is also consistent with the value $\sim 3 \times 10^4\,\text{cm}^{-3}$ expected in the theoretical picture described by Padoan et al. (2014), but an order of magnitude larger than an observational value, $(5 \pm 2) \times 10^3\,\text{cm}^{-3}$, obtained by Kainulainen et al. (2014) for other nearby regions via a novel technique involving column density PDFs.

The average logarithmic slope of the high density tail of the histogram in Fig. 8 is ~ -1, but with considerable uncertainty (values in the range -0.8 to -1.6 are consistent with the data). Taking these values together with the power-law index, $k = 1$, appropriate to critical B-E spheres, Eq. (3) would imply that the slope of the high density tail of the volume-weighted version, $P_V(\rho)$, should be in the range ~ -2.3 to -3.1. These slopes are somewhat steeper than the theoretical asymptotic value of -1.54 (Girichidis et al. 2014) and the values suggested by simulations, which fall in the range $[-7/4, -3/2]$ (Kritsuk et al. 2011). Further progress in comparing the observational characteristics of prestellar cores with theoretical prediction must await a more detailed analysis. Indeed, a fruitful avenue may be to apply our observational core detection procedure directly to the simulated images produced by the gravo-turbulence models.

Previous analyses of the observationally determined density structure of star-forming regions have focused on PDFs of column density rather than volume density. Those PDFs have been characterised by a lognormal at low column densities which becomes dominated by a power law tail at the high end (Kainulainen et al. 2009; Schneider et al. 2013, 2015; Benedettini et al. 2015). The presence of the lognormal component has, however, been questioned by Lombardi et al. (2015) who argue that column density PDFs of molecular clouds can be accounted for entirely by truncated power laws. Conversely, the reality of some of the power-law components has been questioned by Brunt (2015) who has shown that spurious power-law tails can arise if proper account is not taken of noise and warm background components. The PDF of total column density in L1495, shown by the black histogram in Fig. 9 does appear to have distinct power-law behaviour for all but the lowest column densities. To interpret the PDF in light of the various possible effects, it is helfpul to separate the contributions of starless cores and filamentary structure, by replotting the PDF after subtraction of the filamentary background (the *getsources* cleaned background image). The resulting histogram is shown in gold in Fig. 9. It represents the column density PDF associated with compact sources on size scales $\lesssim 4'$ and is seen to be qualitatively similar to the PDF of volume density in Fig. 8. In particular, the high density tail in both cases is fully accounted for by the prestellar cores

---

[6] We do not, of course, assume that all cores have the same density. The distribution of core densities would reflect the range of external pressures.
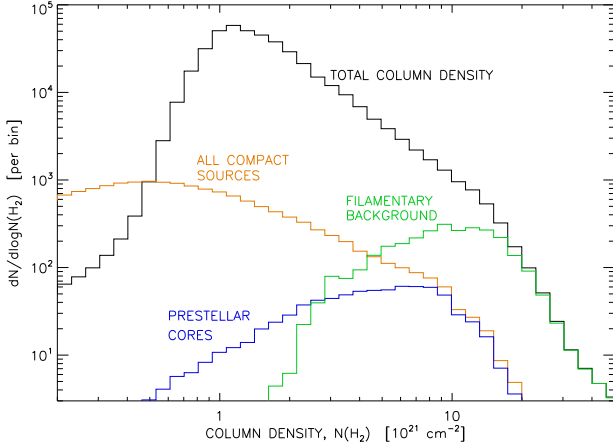
Figure 9. Column density PDFs. The black histogram represents the distribution of total column density values averaged over an effective resolution element of FWHM 18.2″, and is truncated on the left at the approximate level of the noise. The gold histogram represents the distribution after the subtraction of filamentary background, i.e., it represents the net contribution from compact ($\lesssim 4'$) sources in the field. The blue histogram represents the contribution from prestellar cores only. The green histogram represents the distribution of total column density in the immediate vicinity (within two core radii) of prestellar cores, and shows that the highest column densities are dominated by the filamentary backgrounds in those neighbourhoods.

which have been identified via source extraction and whose contribution is shown by the blue histogram in Fig. 9. These tails, therefore, cannot be attributed to artifacts of the type discussed by Brunt (2015).

With regard to the histogram of total column density, Fig. 9 shows that the cores themselves do not account for the highest column densities in the region—the filamentary background is important also, as illustrated by the green histogram in that figure. Although the peak column densities occur at the locations of prestellar cores, the filamentary contribution is dominant at those locations, a situation similar to that in Aquila (Könyves et al. 2015).

7   CONCLUSIONS

The principal conclusions from this study can be summarized as follows:

(i) We have obtained a census of prestellar cores in L1495 (total = 52) which is ~ 85 % complete for $M/M_\odot > 0.1$;

(ii) The overall starless CMF is not well represented by a lognormal function and shows no evidence of a low-mass turnover. Instead, it is consistent with power-law behaviour similar to that shown by clumps seen in various isotopologues of CO;

(iii) The prestellar CMF of L1495 resembles the stellar system IMF as has been found previously for other star-forming regions, albeit with rather low number statistics;

(iv) All of the inferred prestellar cores lie on filamentary structure and the associated background column density distribution is sharply peaked near the critical value for cylindrical stability against gravitational collapse;

(v) The PDF of volume density for starless cores is consistent with the effect of self gravity on magnetized supersonic turbulence. Indeed, it is characterised by a lognormal except for the presence of a high density tail attributable entirely to collapsing prestellar cores. Note that this conclusion applies to the starless core population only and does not include the contribution of the filamentary background.

REFERENCES

André, Ph., Belloche, A., Motte, F., & Peretto, N. 2007, A&A, 472, 519

André, Ph., Men'shchikov, A., Bontemps, S. et al., 2010, A&A, 518, L102

André, Ph., Ward-Thompson, & D., Greaves, J., 2012, Science, 337, 69

André, Ph., Di Francesco, J., Ward-Thompson, D., et al. 2014, in Protostars and Planets VI, Henrik Beuther, Ralf S. Klessen, Cornelis P. Dullemond, and Thomas Henning (eds.), University of Arizona Press, Tucson, 914, pp 27-51

Alves, J., Lombardi, M., Lada, C. J. 2007, A&A, 462, L17

Arzoumanian, D., André, Ph., Didelon, P. et al. 2011, A&A, 529, L6

Benedettini, M., Schisano, E., Pezzuto, S. et al. 2015, MNRAS, 453, 2036

Benson, P. J. & Myers, P. C. 1989, ApJ, 71, 89

Bertoldi, F. & McKee, C. F. 1992, ApJ, 395, 140

Blitz, L. 1993, in Protostars & Planets III, Eds. E. H. Levy and J. I. Lunine (Tucson: Univ. of Arizona Press), p. 125

Bonnor, W. B. 1956, MNRAS, 116, 351

Bernard, J.-P., Paradis, D., Marshall, D. J., et al. 2010, A&A, 518, L88

Brunt, C. M. 2015, MNRAS, 449, 4465

Chabrier, G. 2003, PASP, 115, 763

Collins, D. C., Kritsuk, A. G., Padoan, P. et al. 2012, ApJ, 750, 13

Curtis, E. I., "A Submillimetre Survey of Clustered Low-Mass Star Formation," PhD Thesis, University of Cambridge, 2009

Curtis, E. I., Richer, J. S. & Buckle, J. V. 2010, MNRAS, 401, 455

Doi, Y., Takita, S., Ootsubo, T. et al. 2015, arXiv:1503.06421v1

Ebert, R. 1955, Zeitschrift für Astrophysik, 37, 217

Elias, J. H. 1978, ApJ, 224, 857

Elmegreen, B. G. & Scalo, J. 2004, ARA&A 42, 211

Evans, N. J. II, Rawlings, J. M. C., Shirley, Y. L. & Mundy, L. G. 2001, ApJ, 557, 193

Federrath, C. & Klessen, R. S. 2013, ApJ, 763, 51

Garcia-Lario, P., Lorente, R., Merin, B. et al. 2014, Herschel Observers' Manual, HERSCHEL-HSC-DOC-0876, Version 5.0.3, Chapter 4

Ginsburg, A., Federrath, C., & Darling, J. 2013, ApJ, 779, 50

Girichidis, P., Konstandin, L., Whitworth, A. P., Klessen, R. S. 2014, ApJ, 781, 91

Goldsmith, P. F., Heyer, M., Narayanan, G., et al., 2008, ApJ, 680, 428

Griffin, M. J., Abergel, A., Abreu, A., et al. 2010, A&A, 518, L3

Griffin, M. J., North, C. E., Amaral-Rogers, A. et al. 2013, MNRAS, 434, 992

Hennebelle, P. & Chabrier, G. 2008, ApJ, 684, 395

Hildebrand, R. H. 1983, QJRAS, 24, 267

Hacar, A., Tafalla, M., Kauffmann, J, & Kov'acs, A. 2013, A&A 554, 55

Inutsuka, S. & Miyama, S. M. 1997, ApJ, 480, 6811

Kirk, J. M., Ward-Thompson, D., & André. 2005, MNRAS, 360, 1506

Kirk, J. M., Ward-Thompson, D., Palmeirim, P. et al. 2013, MNRAS, 432, 1424

Kainulainen, J., Beuther, H., Henning, T., & Plume, R. 2009, A&A, 508, L35

Kainulainen, J., Federrath, C. & Henning, T. 2014, Science, 344, 183

Kauffmann, J., Pillai, T., Shetty, R., et al. 2010, ApJ, 716, 433

Könyves, V., André, P., Men'shchikov, A., et al. 2010, A&A, 518, L106

Könyves, V., André, Ph., Men'shchikov, A., et al. 2015, A&A, 584, A91

Kramer, C., Stutzki, J., Rohrig, R., Corneliussen, U. 1998, A&A, 329, 249

Kritsuk, A. G., Norman, M. L., & Wagner, R. 2011, ApJ, 727, L20

Kroupa, P. 2001, MNRAS, 322, 231

Kroupa, P., Weidner, C., Pflamm-Altenburg, J. et al. 2013, in Planets, Stars & Stellar Systems, Vol. 5, Oswalt, T. D. (Editor-in-Chief), Springer

Larson, R. B. 1981, MNRAS, 194, 809

Lombardi, M., Alves, J., & Lada, C. J. 2015, A&A, 576, L1

Lutz, D. 2012, *Herschel* Document PICC-ME-TN-033

Marsh, K. A., Griffin, M. J., Palmeirim, P. et al. 2014, MNRAS, 439, 3683

Men'shchikov, A., André, Ph., Didelon, P. et al. 2012, A&A, 542, 81

Men'shchikov, A. 2013, A&A, 560, A63

Molina, F. Z., Glover, S. C. O., Federrath, C., & Klessen, R. S. 2012, MNRAS, 423, 2680

Motte, F., André, Neri, R. 1998, A&A 336, 150

Onishi, T., Mizuno, A, Kawamura, A et al. 1996, ApJ 465, 81

Onishi, T., Mizuno, A, Kawamura, A et al. 2002, ApJ 575, 950

Ott, S., 2010, in Y. Mizumoto, K.-I. Morita, & M. Ohishi ed., Astronomical Data Analysis Software and Systems XIX Vol. 434 of ASP Conference Series, The *Herschel* Data Processing System – HIPE and Pipelines – Up and Running Since the Start of the Mission, p. 139 Mizuno, A, Kawamura, A et al. 2002, ApJ 575, 950

Padoan, P. & Nordlund, A. 2002, ApJ, 576, 870

Padoan, P., Federrath, C., Chabrier, G. et al. 2014, in H. Beuther, R. S. Klessen, C. P. Dullemond, Th. Henning eds., Protostars and Planets VI, University of Arizona Press, pp.77-100

Palmeirim, P., André, Ph., Kirk, J. et al. 2013, A&A, 550, A38

Poglitsch, A., Waelkens, C., Geis, N., et al. 2010, A&A, 518, L2

Polychroni, D., Schisano, E., Elia, D., et al. 2013, ApJ, 777, L33

Rebull, L. M., Koenig, X. P., Padgett, D. L. 2013, ApJS, 196, 4

Roussel, H. 2013, PASP, 125, 1126

Roy, A., André, Ph., Palmeirim, P., et al. 2014, A&A, 562, 138

Sadavoy, S. I., Di Francesco, J., Bontemps, S., et al. 2010, ApJ, 710, 1247

Schmalzl, M., Kainulainen, J., Quanz, S. P., et al. 2010, ApJ, 725, 1327

Schneider, N., André, Ph., Könyves, V., et al. 2013, ApJ, 766, L17

Schneider, N., Ossenkopf, V., Csengeri, T., et al. 2015, A&A, 575, 79

Simpson, R. J., Nutter, D., Ward-Thompson, D. 2008, MNRAS, 391, 205

Stamatellos, D., Whitworth, A. P. & Ward-Thompson, D. 2007, MNRAS, 379, 1390

White, G. J., Drabek-Maunder, E., Rosolowsky, E. et al. 2015, MNRAS, 447, 1996

APPENDIX A: ESTIMATION OF CATALOGUE COMPLETENESS

The completeness of starless core detection may be estimated by repeating the full source extraction and source classification procedure using simulated data for a set of model cores whose spatial distribution, spatial density, and physical parameters resemble those in the actual L1495
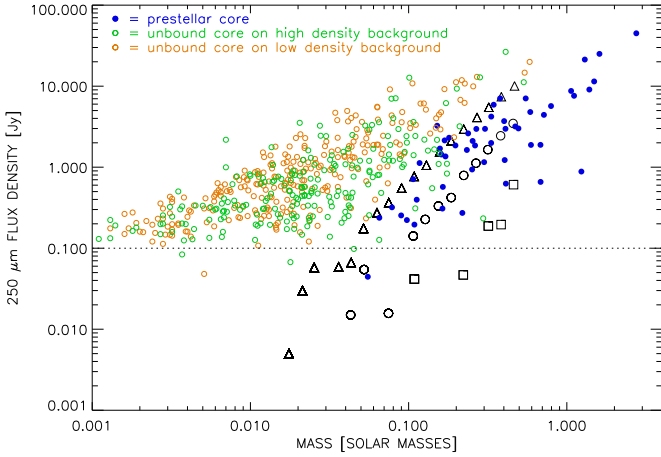
Figure A1. The 250 μm flux densities of observed and model cores as a function of mass. Black symbols represent the model prestellar cores used in the completeness simulation, taken to be critical B-E spheres. They are plotted for three density regimes, indicated by triangles (low density case), open circles (moderate density case) and squares (high density case). Also shown for comparison are the observational values for the extracted sources, represented by the coloured symbols. These are divided into prestellar cores (blue filled circles), and gravitationally unbound cores (open circles, where green and gold designate those seen against high and low column density backgrounds, respectively, based on a threshold of $A_V = 7$ mag). For reference, the horizontal dotted line represents the approximate flux density sensitivity limit.

cloud. In doing so, one must consider that the detectability of a core is not fully characterised by its mass. The mean dust temperature is another important factor and that quantity is, in turn, determined by other physical parameters whose distributions can lead to different possible flux densities for a given mass. In particular, the cooler and more highly condensed prestellar cores have different detectability characteristics from those of the general unbound starless population which is more diffuse. We have therefore modelled the completeness of those two object types separately.

Following Könyves et al. (2015), we have modelled the bound (prestellar) cores as critical B-E spheres. The radial temperature distribution was determined from a dust radiative transfer model (Men'shchikov et al., in preparation). Three populations of bound cores were generated, characterised by median central density values of approximately 4×10^6 cm^{-3} (low density set), 2×10^7 cm^{-3} (moderate density set), and 6×10^7 cm^{-3} (high density set), with a wide range (4–5 orders of magnitude) within each set. In all cases, the cores were embedded in a cloud with $A_V = 3.7$ mag. The behaviour of 250 μm flux density as a function of mass for the three sets is shown in Fig. A1 and may be compared with the observed values of extracted prestellar cores.

With regard to the unbound starless cores, Fig. A1 shows that these objects are detected at masses considerably below those of prestellar cores, both in regions of high and low column density. Many of these objects are probably transient structures which are not only gravitationally unbound but may also not even be pressure confined. Their importance to star formation studies lies in the fact that,

in terms of mass distribution, they appear to form a continuous sequence that includes prestellar cores. The latter objects represent the upper end of the mass range, defined by the point at which self-gravity becomes dominant. The unbound cores may therefore provide useful constraints on dynamical models of the interstellar turbulence that gives rise to the prestellar subset.

At the low end of the mass range ($M \lesssim 0.1\,M_\odot$), all of the detected objects are either unresolved or marginally resolved and hence for a given mass and background rms, the only quantity which determines detectability is then the dust temperature. As discussed earlier, Fig. 4 suggests a negative correlation between mass and temperature although, given the detection limits, it is not clear that the correlation persists down to the lowest masses. However, if we assume that the lowest-mass condensations are diffuse, then their dust temperatures can be expected to be systematically high due to easier penetration by the ISRF, and hence be more detectable than a prestellar core of the same mass. For larger masses and hence larger radii, however, cores become spatially resolved and detectability is then determined by the peak contrast, $N_{H_2}^{pk}/N_{bg}$, of column density with respect to the local background. In that regime, a prestellar core becomes more detectable than an unbound core of the same mass.

It is, of course, possible that the detected objects are not representative of the entire population of unbound starless cores. For example, the detection limit in Fig. 4 leaves open the possibility of a large population of cool objects of low mass. Likewise, we cannot rule out the existence of a substantial population of objects of very low density contrast, at all sizes, which are not detected by *getsources*. In order to provide a meaningful definition of completeness for unbound starless cores, we therefore need a more precise observational definition. So as a working set of criteria, we take such objects to be gravitationally unbound condensations whose sizes are approximately consistent with the Larson (1981) mass-radius relation and whose dust temperatures are consistent with the mass-temperature behaviour shown in Fig. 4. We have made an assessment of the detection completeness of such objects using simulations based on empirically determined values of physical parameters. The latter were based on the following functional forms, adapted from Marsh et al. (2014), for the radial dependence of molecular hydrogen number density, $n(r)$, and dust temperature, $T(r)$, assuming spherical symmetry:

$$n(r) = n_0/[1 + (r/r_0)^2] \tag{A1}$$

$$T(r) = T_0 + (T_{out} - T_0)r/r_{out} \tag{A2}$$

where r_0 represents the radius of an inner plateau, r_{out} is the outer radius of the core, T_0 is the central core temperature, and T_{out} is the temperature at the outer radius. In relating $n(r)$ to the corresponding profile of mass density, we assumed a mean molecular weight, μ, of 2.8 (Roy et al. 2014). The assumed mass distribution was based on the Kroupa (2001) IMF, and the slope of the mass-radius relation was taken as 1.9 (Larson 1981). The relative values of r_0 and r_{out} and their statistical dispersions were based on the results of Marsh et al. (2014). The temperatures T_0 and T_{out} were also based on the latter results, with a constant value of 11 K assumed for T_{out}. The emergent intensity was then calculated using the opacity law given by Eq. (1).

Using the above source models, we have constructed synthetic images for 384 critical B-E cores and 600 additional objects whose parameter values were based on empirical data. The latter subset was designed to represent the general unbound starless population. Each model image was convolved with the *Herschel* beam at the corresponding wavelength using published beam data. Specifically, the PACS beams were obtained by azimuthal averaging the observationally determined PSFs from Lutz (2012). For SPIRE, azimuthally symmetric PSFs were obtained using the radial profiles from Griffin et al. (2013). The model images were then sprinkled onto noisy backgrounds corresponding to the *getsources* cleaned background images (Men'shchikov et al. 2012) at the five wavelengths. They were distributed randomly over the portions of the image dominated by dense filamentary material which, for the empirically-modelled objects, were taken as the regions in which the 250 μm background intensity exceeded 57 MJy sr^{-1} after applying the Planck offset correction. This intensity level corresponds to $A_V \lesssim 5$ mag over most of the region. The B-E population, on the other hand, was distributed over the regions for which the local column density exceeded 5×10^{21} cm^{-2} ($A_V > 5$ mag). Fig. A2 shows the simulated 250 μm image together with the locations of the model sources.

Having thus generated synthetic images at the five wavelengths for the same $4° \times 2°$ field as the *Herschel* observations, the same source detection and classification procedure, as discussed in Section 2, was used to produce a set of core candidates—their locations are also indicated in Fig. A2. Comparison of recovered sources with the "truth" table from the simulations enabled completeness curves to be derived. These curves were derived separately for the unbound and bound cores and the results are shown in Fig. A3. In the case of unbound cores, the completeness curve is representative of moderate backgrounds for which $A_V \lesssim 5$ mag. The error bars represent Poisson errors only and do not incorporate the additional effects of model errors which are difficult to quantify. But subject to that caveat, we estimate that our census of unbound cores is $\sim 85\%$ complete for $M/M_\odot > 0.015$ at $A_V \lesssim 5$ mag.

For the prestellar cores we have compared the results of our numerical simulation with the predicted completeness obtained from the model described in Appendix B.2 of Könyves et al. (2015), which is based on critical B-E spheres. The predicted curve for L1495 is indicated by the black dashed curve in Fig. A3 and is seen to be quite consistent with the simulation. Since this curve is model-based it represents *true* mass as opposed to observationally derived mass, the latter of which may be systematically underestimated by up to a factor of 2 as discussed in Section 6. Based on these results we estimate that the census of bound cores is $\sim 85\%$ complete for $M/M_\odot > 0.1$.

APPENDIX B: THE CATALOGUE AND DERIVED CORE PROPERTIES

Tables B1 and B2 show example portions of the dense core catalogue and the derived properties for dense cores, respectively. The complete tables are available in the on-line ver-
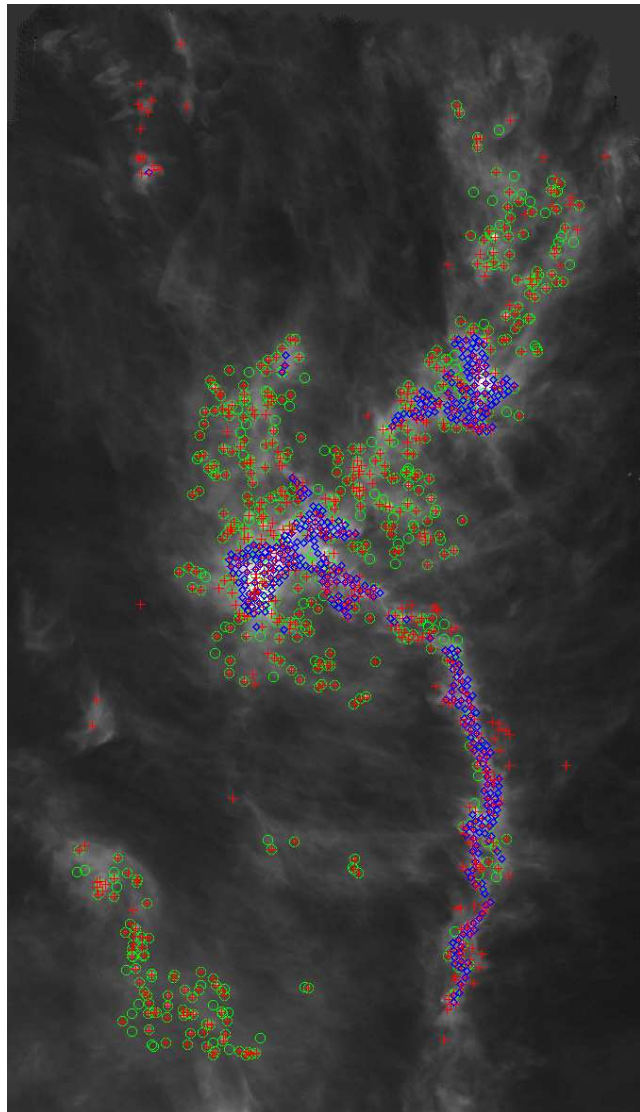
Figure A2. Simulated SPIRE 250 μm image, used for evaluation of the catalogue completeness. The field dimensions and intensity scale are the same us for Fig. 1. Green circles represent empirically modelled cores which may be interpreted as the dust-emission counterparts of CO clumps, blue diamonds represent bound (prestellar) model cores, and red crosses represent core candidates extracted from the simulated data.

sion of the paper[7]. The quoted values of integrated flux for non-detections are, in some cases, negative, particularly at 70 μm wavelength. Such values, in conjunction with their standard deviations, convey statistical information necessary for optimal fitting of SEDs using the maximum likelihood criterion. They can also be physically meaningful since, e.g., starless cores can be seen in absorption against a warmer background at 70 μm.

In addition to starless cores, both tables contain entries for dense cores in which protostars are embedded. For present purposes, an embedded core is defined as one in which a significant compact source of 70 μm emission is

---

[7] The tables are also available, together with the full set of HGBS data products, from http://gouldbelt-herschel.cea.fr/archives

Figure A3. Catalogue completeness as a function of mass based on simulated data for unbound cores and bound (prestellar) cores, represented by the red and blue curves, respectively. Error bars represent Poisson statistics only. The curve for unbound cores is representative of moderate ($A_V \lesssim 5$ mag) backgrounds. In that regime, low mass unbound cores ($M/M_\odot < 0.1$) are more easily detectable than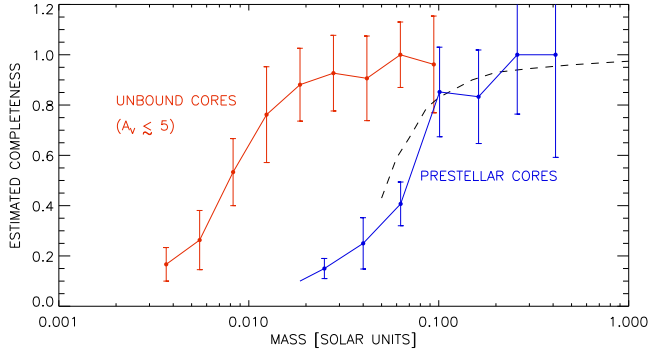 their prestellar counterparts due to their systematically higher temperatures. The simulated completeness for prestellar cores may be compared with the expected behaviour based on the model described by Könyves et al. (2015), indicated by the black dashed curve.

present within its 50% column density contour. Their derived properties are more uncertain and their masses may be underestimated by a factor of ~ 2. We detect 11 such objects in L1495. They are not considered further in the present work, but will be discussed in a forthcoming paper.

The rightmost column of Table B1 indicates matches with objects listed in the SIMBAD database and includes several previous surveys of dense cores. In most cases, those surveys were made at lower resolution and typically have blended the core either with neighbouring cores or with associated background filamentary structure. One example is LDN 1495N, whose mass and radius are listed as 1.85 $M_\odot$ and 0.07 pc, respectively, in the NH$_3$ survey of Benson & Myers (1989), whereas the corresponding *Herschel* values are 1.39 $M_\odot$ and 0.050 pc, respectively. More extreme examples are to be found in comparisons with the C^{18}O catalogue of Onishi et al. (1996), in which objects 2, 3, and 11 have masses in the range 16.6–46.0 $M_\odot$, considerably in excess of their *Herschel* counterparts. A closer correspondence is found between our *Herschel* cores and the H^{13}CO$^+$ cores of Onishi et al. (2002), as discussed by Marsh et al. (2014).

Comments in the far right column of Table B2 indicate failed SED fits (see Section 4). They also indicate cases in which the source was spatially unresolved in column density. In those cases, the mean peak column densities and volume densities were derived using the observed source size only.

Table B1. Catalogue of dense cores in L1495. The full table is presented in the on-line version of the paper. A portion is reproduced here to show form and content.

Src#[a]	Source name[b] HGBS_J*	RA$_{2000}$ [h m s]	Dec$_{2000}$ [° ′ ″]	(Sig$_{70}$)[c]	(I_{70}^{pk})[d] [Jy/beam]	$\sigma(I_{70}^{pk})$[e] [Jy/beam]	(I_{70}^{pk}/I_{bg})[f]	$(I_{070}^{conv,500})$[g] [Jy/beam$_{500}$]	(S_{70})[h] [Jy]	$\sigma(S_{70})$[i] [Jy]	(a_{70})[j] [″]	(b_{70})[k] [″]	(PA$_{70}$)[l] [°]	Cont'd →
1	040924.1+284723	04 09 24.10	+28 47 23	0.9	-3.81e-03	4.3e-03	0.00	-5.55e-02	5.41e-04	2.2e-02	85	44	77	
17	041042.8+281925	04 10 42.84	+28 19 25	0.0	2.92e-02	1.2e-02	0.00	2.29e-02	8.02e-02	3.4e-02	29	27	50	
76	041335.4+282117	04 13 35.45	+28 21 17	2.4	-1.59e-02	6.7e-03	0.00	-3.00e-01	4.13e-01	7.8e-02	143	116	153	
421	041840.7+281916	04 18 40.67	+28 19 16	2245.0	2.94e+01	5.5e-02	38.12	3.49e+01	5.16e+01	1.1e-01	9	8	159	

Sig$_{160}$	I_{160}^{pk} [Jy/beam]	$\sigma(I_{160}^{pk})$ [Jy/beam]	I_{160}^{pk}/I_{bg}	$I_{160}^{conv,500}$ [Jy/beam$_{500}$]	S_{160} [Jy]	$\sigma(S_{160})$ [Jy]	a_{160} [″]	b_{160} [″]	PA$_{160}$ [°]	Sig$_{250}$	I_{250}^{pk} [Jy/beam]	$\sigma(I_{250}^{pk})$ [Jy/beam]	I_{250}^{pk}/I_{bg}	$I_{250}^{conv,500}$ [Jy/beam$_{500}$]	S_{250} [Jy]	$\sigma(S_{250})$ [Jy]	a_{250} [″]	b_{250} [″]	PA$_{250}$ [°]	Cont'd →
6.5	1.04e-01	2.6e-02	0.56	5.04e-01	1.02e+00	8.1e-02	56	35	56	8.8	2.13e-01	3.5e-02	1.07	0.483	1.34e+00	8.1e-02	44	34	132	
0.0	1.87e-02	2.2e-02	0.00	3.47e-02	4.33e-02	3.8e-02	20	17	69	8.1	1.97e-01	3.0e-02	0.46	0.330	3.98e-01	3.1e-02	32	24	82	
6.1	9.87e-03	2.3e-02	0.00	6.44e-02	1.62e+00	1.1e-01	176	53	86	18.8	6.37e-01	5.4e-02	1.47	1.996	1.14e+01	2.7e-01	72	63	27	
927.9	2.13e+01	4.5e-01	6.91	2.32e+01	2.06e+01	5.3e-01	14	14	90	670.8	1.06e+01	5.5e-01	3.11	10.174	7.08e+00	4.8e-01	18	18	128	

Sig$_{350}$	I_{350}^{pk} [Jy/beam]	$\sigma(I_{350}^{pk})$ [Jy/beam]	I_{350}^{pk}/I_{bg}	$I_{350}^{conv,500}$ [Jy/beam$_{500}$]	S_{350} [Jy]	$\sigma(S_{350})$ [Jy]	a_{350} [″]	b_{350} [″]	PA$_{350}$ [°]	Sig$_{500}$	I_{500}^{pk} [Jy/beam]	$\sigma(I_{500}^{pk})$ [Jy/beam]	I_{500}^{pk}/I_{bg}	S_{500} [Jy]	$\sigma(S_{500})$ [Jy]	a_{500} [″]	b_{500} [″]	PA$_{500}$ [°]	Cont'd →
12.7	2.72e-01	6.9e-02	1.11	4.25e-01	1.17e+00	1.2e-01	50	41	134	13.8	2.34e-01	5.8e-02	0.67	5.11e-01	6.8e-02	57	43	135	
11.6	2.88e-01	5.3e-02	0.60	3.31e-01	4.05e-01	4.8e-02	34	25	68	14.0	2.20e-01	7.3e-02	0.50	3.23e-01	6.7e-02	55	37	80	
32.3	9.26e-01	7.6e-02	1.41	1.73e+00	1.06e+01	2.8e-01	81	68	168	41.4	9.52e-01	7.4e-02	0.76	5.24e+00	1.6e-01	103	61	152	
348.6	5.24e+00	7.2e-01	1.83	5.21e+00	4.40e+00	6.6e-01	25	25	147	157.5	2.36e+00	8.2e-01	0.96	1.88e+00	7.5e-01	36	36	158	

Sig(N_{H_2})[m]	$(N_{H_2}^{pk})$[n] [10^{21} cm^{-2}]	$(N_{H_2}^{pk}/N_{bg})$[o]	$(N_{H_2}^{conv,500})$[p] [10^{21} cm^{-2}]	$(N_{H_2}^{bg})$[q] [10^{21} cm^{-2}]	$(a[N_{H_2}])$[r] [″]	$(b[N_{H_2}])$[s] [″]	(PA$[N_{H_2}]$)[t] [°]	N_{SED}[u]	CSAR[v]	Core type[w]	SIMBAD[x]	Comments
8.4	0.8	0.25	2.2	11.4	56	35	119	4	1	1		
13.2	1.7	0.62	2.8	16.1	33	18	41	4	0	3		
62.3	6.7	0.93	23.6	33.4	81	58	145	4	1	2	[OMK2002] 3	
73.9	7.5	1.04	9.3	28.2	22	18	157	5	1	4	V892 Tau	

[a] Source number in catalogue.

[b] Source name. The full name consists of the prefix "HGBS_J" followed directly by the tabulated label created from J2000 sexagesimal coordinates.

[c] Detection significance from monochromatic single scales in the image at the specified wavelength. Non-detections are labelled as 0.0.

[d] Estimate of the peak intensity.

[e] Uncertainty in peak intensity.

[f] Contrast of the peak intensity over the local background.

[g] Peak intensity after smoothing to a 36″3 beam.

[h] Estimate of the total flux and its uncertainty.

[i] Uncertainty in total flux.

[j] Estimate of source size (FWHM) along major axis.

[k] Estimate of source size (FWHM) along minor axis.

[l] Position angle of source major axis, east of north.

[m] Detection significance from single scales on high-resolution column density map.

[n] Peak column density.

[o] Contrast of peak column density over the local background.

[p] Peak column density after smoothing to a 36″3 beam.

[q] Local background column density.

[r] FWHM along major axis in column density.

[s] FWHM along minor axis in column density.

[t] Position angle of major axis in column density.

[u] Number of *Herschel* bands in which the source is significant (Sig$_\lambda > 5$) and has a positive flux density, excluding the column density plane.

[v] Equal to 1 if source found independently by CSAR, and 0 otherwise.

[w] 1=starless(unbound); 2=prestellar; 3=candidate prestellar; 4=dense core with embedded protostar.

[x] SIMBAD association: ID of nearest match if within 1′ of *Herschel* position. A key to the abbreviations used is given in the online version.

Table B2. Derived properties of dense cores in L1495. The full table is presented in the on-line version of the paper. A portion is reproduced here to show form and content.

Src#[a]	Source name[b] HGBS_J*	RA$_{2000}$ [h m s]	Dec$_{2000}$ [° ′ ″]	(R_c^{obs})[c] [pc]	(R_c^{dec})[d] [pc]	(M_c)[e] [$M_\odot$]	(σM_c)[f] [$M_\odot$]	(T_d)[g] [K]	(σT_d)[h] [K]	$(N_{H_2}^{pk})$[i] [$10^{21}\,cm^{-2}$]	$(\bar{N}_{H_2}^{obs})$[j] [$10^{21}\,cm^{-2}$]	$(\bar{N}_{H_2}^{dec})$[k] [$10^{21}\,cm^{-2}$]	$(n_{H_2}^{pk})$[l] [$10^4\,cm^{-3}$]	$(\bar{n}_{H_2}^{obs})$[m] [$10^4\,cm^{-3}$]	$(\bar{n}_{H_2}^{dec})$[n] [$10^4\,cm^{-3}$]	(α_{BE})[o]	Core type[p]	Comments
1	040924.1+284723	04 09 24.10	+28 47 23	0.030	0.027	0.040	0.009	12.4	0.5	0.8	0.63	0.78	0.7	0.51	0.71	13.8	1	
17	041042.8+281925	04 10 42.84	+28 19 25	0.017	0.015	0.061	0.027	8.9	0.7	2.2	3.13	3.73	2.2	4.55	5.93	3.7	3	
76	041335.4+282117	04 13 35.45	+28 21 17	0.046	0.045	1.488	0.243	8.7	0.2	41.1	9.86	10.67	23.4	5.17	5.82	0.4	2	
421	041840.7+281916	04 18 40.67	+28 19 16	0.013	0.010	0.026	0.008	22.9	2.2	2.4	2.02	3.80	3.0	3.66	9.43	14.4	4	

[a] Source number in catalogue

[b] Source name. The full name consists of the prefix "HGBS_J" followed directly by the tabulated label created from J2000 sexagesimal coordinates.

[c] Core radius as observed, derived from the high-resolution (18″.2) column density map, assuming 140 pc distance.

[d] Core radius, beam-deconvolved; derived from the high-resolution (18″.2) column density map, assuming 140 pc distance.

[e] Estimated core mass.

[f] Uncertainty in core mass.

[g] Estimated dust temperature.

[h] Uncertainty in dust temperature.

[i] Peak H_2 column density at the resolution of the 500 μm data, derived from a modified blackbody SED fit to the core peak flux densities measured in a common 36″.3 beam at all wavelengths.

[j] Average column density, derived from the estimated mass and radius *before* deconvolution.

[k] Average column density, derived from the estimated mass and radius *after* deconvolution.

[l] Beam-averaged peak volume density at the resolution of the 500 μm data, derived from the peak column density on the basis of an assumed Gaussian source profile, using: $n_{H_2}^{pk} = \sqrt{4\ln 2/\pi}\; N_{H_2}^{pk}\,/\,FWHM_{500}$.

[m] Average volume density, based on the estimated radius *before* deconvolution, using: $\bar{n}_{H_2}^{obs} = M_c/(\frac{4}{3}\pi R_c^3 \mu m_H)$, where $\mu = 2.8$.

[n] Average volume density, based on the estimated radius *after* deconvolution, but otherwise using the same equation.

[o] Bonnor-Ebert mass ratio, $\alpha_{BE} = M_{BE}/M_c$ (see Section 4).

[p] 1=starless(unbound); 2=prestellar; 3=candidate prestellar; 4=dense core with embedded protostar.

This paper has been typeset from a TEX/ LATEX file prepared
by the author.